Atmospheric correction of OLCI imagery over very turbid waters based on the RED/NIR/SWIR bands

Juan I. Gossn
Quantitative Remote Sensing Team
Marine Division
Instituto de Astronomía
y Física del Espacio
Buenos Aires, Argentina
Email: gossn@iafe.uba.ar

Kevin G. Ruddick
Remote Sensing and Ecosystem Modelling
Operational Directorate Natural Environment
Royal Belgian Institute of
Natural Sciences
Brussels, Belgium
Email: kruddick@naturalsciences.be

Ana I. Dogliotti
Quantitative Remote Sensing Team
Marine Division
Instituto de Astronomía
y Física del Espacio
Buenos Aires, Argentina
Email: adogliotti@iafe.uba.ar

Abstract—The standard NASA atmospheric correction using near infrared bands (700 nm - 900 nm) may work for clear to moderately turbid waters, but generally fails for extreme turbidities because of flattening of the water reflectance spectrum. The use of SWIR bands at 1.6 μm and/or 2.3 μm, such as the bands present on MODIS, can be effective in extremely turbid waters, but may not be present, such as in the case of OLCI (Sentinel 3A), where a new SWIR band at 1016 nm is placed instead. This band may help to improve atmospheric correction in turbid waters at a lower marginal cost than longer SWIR bands. In this work, we endeavored to find "atmospheric invariant" quantities using the RED/NIR/SWIR bands on OLCI to construct an atmospheric correction scheme over turbid waters. We found that if we choose certain spectrally-close band triplets (such as OLCI bands at 709-779-865 nm), the Rayleigh-corrected reflectance of the triplet's "middle" band after baseline subtraction (or baseline residual, BLR) is essentially independent of the atmospheric conditions (including for very hazy scenes). In this work, we used three consecutive band triplets of the group of bands 620-709-779-865-1016 nm to construct the three corresponding BLRs and relate them to water reflectances at these wavelengths. To establish this relation, we used a simple water reflectance model for turbid scenarios where we varied backscattering and absorption properties according to previously reported values and the spectral behaviour of in-situ radiometric data from Río de la Plata (Argentina). We also tested the algorithm on a simulated dataset, obtaining good performances (almost 1:1 relation and $R^2 \geq 97\%$) for scenarios without direct sunglint.

Index Terms—atmospheric correction, turbid waters, OLCI

I. INTRODUCTION

The NASA standard atmospheric correction algorithm applied to MODIS (Moderate Resolution Imaging Spectroradiometer) imagery uses two bands in the NIR (Near Infra-Red) at 765 and 865 nm, assuming zero water-leaving radiance contribution (black pixel) at these bands [9]. The process consists on i) estimating the atmospheric component from these bands (taking advantage of the absence of marine signal), and ii) extrapolating the signal to the VIS (visible) bands. For cases with a moderate but non-negligible marine signal in the NIR, an iterative process is run to estimate this component, subtract it from the total signal to recover the black pixel condition, and proceed as usual for the extrapolation to the

VIS [22]. In waters with high concentrations of suspended particulate matter (SPM), which backscatter in the NIR, the signal at 765 and 865 nm is not moderate anymore and even exceeds sometimes the saturation values of the sensor [5]. In these cases, this iterative procedure no longer works and other alternatives are needed. An alternative was proposed in which the black pixel assumption was assumed on the Short-Wave-Infra-Red (SWIR) bands (e.g. 1240, 1640 and 2130 nm in MODIS), where water absorption drastically increases making the black pixel assumption still hold, [23] even in highly turbid waters scenarios.

ESA's Ocean and Land Colour Instrument (OLCI) on Sentinel 3A incorporates a SWIR-band at 1016 nm instead, which adds significant information on sediment content of water, but where black-pixel assumption does not hold for extreme turbidities [11]. Due to this novel spectral band, OLCI imagery provide an opportunity to test alternatives to SWIR-based approaches for turbid water atmospheric correction.

In this work, we endeavored to find "atmospheric invariant" quantities using the RED-NIR-SWIR (RNS) bands on OLCI to construct an atmospheric correction scheme over turbid waters. It is based on the fact that in the RNS region, atmospheric reflectance is markedly smoother (spectrally) than turbid water reflectances. Information provided by the MERIS-heritage bands at 620, 709, 779 and 865 nm together with the new band at 1016 nm might be used to exploit these spectral differences. The reflectance peak after baseline correction or "Baseline Residual" (BLR), like the Fluorescence Line Height product [13], provides an effective means to remove atmospheric effects, and can be applied to Rayleigh-corrected (RC) reflectances (without prior aerosol correction).

This work explores the potential of considering simultaneously three different BLRs, defined by the RC reflectances at triplets (620-709-779) nm, (709-779-865) nm and (779-865-1016) nm, as aerosol-independent quantities that can be used to infer the water signal on a pixel-by-pixel basis in the RED, NIR and SWIR bands.

This approach can then be used to subtract the water signal and infer an aerosol reflectance in the aforementioned bands to then extend it to the visible bands by a standard extrapolation

procedure such as in [9]. Once these water reflectances are obtained from the image, they can be used to obtain products such as turbidity [6] [7] or total suspended matter [19] [16].

II. Algorithm Description

A. Algorithm Theoretical Basis

In previous works, the combination of Rayleigh corrected (RC) reflectances from three bands was used to quantify different magnitudes without the need of an aerosol correction. Two examples are the Fluorescence Line Height [13] and the Floating Algal Index [10]. Both indexes are defined using the RC reflectance of the middle (M) band (i.e. of intermediate wavelength in the triplet) after having subtracted the value of the baseline formed by the left (L) and right (R) RC reflectances at this middle wavelength. In the present work, this magnitude is denominated Baseline Residual (BLR) and, in the case of RC reflectances, can be expressed as:

$$BLR(\rho_{RC})[L, M, R] = \rho_{RC}[\lambda_M] - BL[\lambda_M] \qquad (1)$$

where L, M, R stands for the Left-Middle-Right triplet, $\rho_{RC}[\lambda_M]$ is the RC reflectance at λ_M and $BL[\lambda_M]$ is the baseline term, given by:

$$BL[\lambda_M] = \frac{\rho_{RC}[\lambda_L](\lambda_M - \lambda_R) + \rho_{RC}[\lambda_R](\lambda_L - \lambda_M)}{\lambda_L - \lambda_R} \qquad (2)$$

The significance of BLRs computed from spectrally-close RC reflectances at bands above 600 nm (i.e., the spectral region that concerns us) is that they are essentially unaffected by the atmospheric components of the signal. To show this, consider the following expression for RC reflectance:

$$\rho_{RC}[\lambda] = \rho_a[\lambda] + \rho_{ra}[\lambda] + T[\lambda]\rho_g + t[\lambda]\rho_w[\lambda] \qquad (3)$$

where each term accounts for photons that arrived at the sensor after: being scattered by aerosols only (ρ_a); being scattered by aerosols and air molecules (ρ_{ra}); being specularly reflected by the water surface (sunglint) ($T[\lambda]\rho_g$, where $T[\lambda]$ is the direct atmospheric transmittance), and having interacted with the in-water components ($t[\lambda]\rho_w[\lambda]$, where $t[\lambda]$ is the diffuse atmospheric transmittance).

Based on typical aerosol types and concentrations such as the modes considered in the WMO models [24], the aerosol reflectances are monotonically decreasing with wavelength [9]. In particular, in a sufficiently short spectral range, e.g. 250 nm in the RNS, the aerosol reflectance can be approximated as a linear-decreasing function of wavelength:

$$\rho_a(\lambda_{i=L,M,R}) \approx \rho_a(\lambda_L). \left[1 - c\frac{\lambda_i - \lambda_L}{\lambda_L}\right] \qquad (4)$$

where c is related to the aerosol type and $\rho_a(\lambda_L)$ is the amplitude at λ_L. If this approximation holds, the aerosol term in Eq. 4 does not contribute to $BLR(\rho_{RC})[L, M, R]$. Rayleigh-aerosol coupling is a very small term for wavelengths above 600 nm, and could also be considered as a near-linear term in a short spectral range, i.e. $BLR(\rho_{ra}) \approx 0$.

Sunglint term is essentially a white term, especially in the RNS region, where molecular scattering is smaller than in the blue, meaning $T[\lambda] \approx 1$, thus $\frac{\partial(T[\lambda]\rho_g)}{\partial\lambda} \approx 0$, i.e. negligible contribution to $BLR(\rho_{RC})$. Thus, considering any triplet of spectrally close bands in the RNS implies a near-linear spectral dependence of the atmospheric-interface terms in the RC reflectance decomposition. Thus the $BLR(\rho_{RC})$ is mainly depending on the water term:

$$BLR(\rho_{RC})[L, M, R] \approx BLR(t.\rho_w)[L, M, R] \qquad (5)$$

The diffuse transmittance factor in Eq. 5, accounts for the fact that photons that have effectively interacted with the in-water constituents might also interact with atmospheric components. Since it is a second order factor, we assume a white diffuse transmittance inside each band triplet:

$$BLR(\rho_{RC})[L, M, R] \approx t[\lambda_M].BLR(\rho_w)[L, M, R] \qquad (6)$$

where $t[\lambda_M]$ is the transmittance factor at λ_L, which we expect to be less than (but close to) 1. The idea of this work is to: i) compute $BLR(\rho_{RC})[L, M, R]$, and ii) exploit Eq. 6 by computing pre-simulated values for $t[\lambda_M]$ (§III-A) and finding an algorithm that relates $BLR(\rho_w)$ to water reflectance.

B. $BLR(\rho_w)$ vs. ρ_w relation

The algorithm uses three band triplets to relate the corresponding three $BLR(\rho_w)$ with water reflectances. The triplets we chose are given by three successive combinations of the following five OLCI bands: $620\,nm, 709\,nm, 779\,nm, 865\,nm$ and $1016\,nm$. From these 5 bands we obtain 3 successive linearly independent RC BLRs: $BLR(\rho_{RC})[620, 709, 779]$, $BLR(\rho_{RC})[709, 779, 865]$ and $BLR(\rho_{RC})[779, 865, 1016]$. These bands have been chosen for the following reasons. Firstly, water reflectance in these bands is markedly more sensitive to the presence of highly-scattering sediments (scenarios of interest) than at lower wavelengths, and has a high spectral variability due to the increasing water absorption as wavelength increases [21]. This means that we expect a high variation of the BLR signal with varying water reflectance. Second, other OLCI bands inside this spectral region are affected by absorption of major atmospheric components such as O_2 (oxygen) and H_2O (water vapour). Third, it is desirable that the atmospheric components affecting the signal (air molecules, aerosols) have a minor impact on the fraction of photons that has interacted with in-water constituents and reaches the sensor. Air molecules (and usually aerosols as well) contain lower scattering cross sections in this spectral region than at lower wavelengths [9]. This means that the chance of photons interacting with the atmosphere before/after having interacted with the in water constituents is minimized, i.e., transmittance factors get closer to unity. Thus, the relation between $BLR(\rho_{RC})$ and $BLR(\rho_w)$ is better established, this means, less affected by the transmittance factor (Eq. 6).

To establish the relation between the $BLR(\rho_w)$ and ρ_w, we use a simple water reflectance model in the RNS:

$$\rho_w[\lambda] = \gamma \frac{b_{bp}[\lambda]}{b_{bp}[\lambda] + a_p[\lambda] + a_w[\lambda]} \qquad (7)$$

where $\gamma = \pi \Re f'/Q \approx 0.216$, considering the factor $\Re = 0.529$ from Loisel and Morel (2001) [14] and the factor $f'/Q = 0.13$ from Morel and Gentili (1996) [17]; $a_w[\lambda]$ and $a_p[\lambda]$ are the absorption coefficients for water and particulate matter, and $b_{bp}[\lambda]$ is the backscattering coefficient for particulate matter. Notice that no term for phytoplankton or CDOM content are introduced in Eq. 7 since their contribution is either negligible or too small in the RNS when considering highly turbid scenarios. Also water backscattering can be considered negligible in this spectral region.

We will assume that the IOPs of particles are proportional to their concentration, S, but establishing an extra factor of variability for absorption, X:

$$b_{bp}[\lambda] = Sb_{bp}^*[\lambda], \qquad a_p[\lambda] = X.Sa_p^*[\lambda] \qquad (8)$$

where the quantities with "*" represent mass-specific IOPs. The spectral shapes of these specific IOPs were taken from Babin *et al.* 2003(a & b) [1] [2], since they are based on mean values of representative coastal areas around Europe. For specific absorption an exponential decay-law is used: $a_p[\lambda(nm)] = a_p[443]exp\{-S_{ap}(\lambda - 443)\}$, where $a_p[443] = 0.036 m^2/g$ and $S_{ap} = 0.0123 nm^{-1}$. Particulate backscattering is derived assuming it is 2% of the total scattering [15], $b_{bp} = 0.02b_p$, and a power-law for the attenuation coefficient (recall $b_p = c_p - a_p$): $c_p[\lambda(nm)] = (a_p[555] + b_p[555])(\frac{\lambda}{555})^{-\gamma_c}$, where $b_p[555nm] = 0.51 m^2/g$ and $\gamma_c = 0.3749$. The extra parameter X is in agreement with the hysteresis process between S and water reflectance in the NIR found by Pinet *et al.* 2017 [20] in the annual cycle of the Madeira River (Amazonas tributary), which was found to be due to a large variability on the specific absorption of particles with their composition, especially in the NIR bands. This is also in agreement with the behavior of $BLRs(\rho_w)$ and $BLRs(\rho_{RC})$ from in-situ data and OLCI imagery (§IV-A).

Once this reflectance model is established, we can generate a look-up-table of values of $BLR(\rho_w)$, where:

$$BLR(\rho_w) = f[S, X] \qquad (9)$$

which are generated applying Eq. 1 on modelled water reflectances (Eq. 7-8) and using OLCI's Spectral Response Functions (SRF) [8]. The LUT produced assumed S varying in $[0 - 1000] \, mg/l$ and X varying between 0.6 and 1.4 ($a_p^*[443]$ varies in $\pm 40\%$ the original value).

On each image, the three computed $BLR(\rho_{RC})$ for each pixel are divided by the three corresponding transmission factors $t[\lambda_M]$ (Eq. 6) and related to the modelled $BLR(\rho_w)[S, X]$ that minimizes the Eulerian distance in BLR 3D space. Hence, from the corresponding $[S, X]$ pair, a particular water reflectance spectrum in the RNS region is retrieved. This approach may be extended to the whole visible range by subtracting the water signal retrieved and applying the clear pixel assumption [9] [22].

CNES-SOS Input Parameter	Inserted Values
λ (Wavelength)	600:3:1100 nm
θ_s (Solar zenith angle)	0°:15°:60°
θ_v (Viewing zenith angle)	0°:15°:60°
$\Delta\varphi$ (Relative azimuth angle)	0°:45°:180°
$\tau_{RAY}[\lambda]$ (Rayleigh Opt. Thickness)	Bodhaine et al. 1999
$\delta_{RAY}[\lambda]$ (Molecular depolarization factor)	Bodhaine et al. 1999
H_{RAY} (Molecular height e-folding)	8 km
dV/dlnr (Aerosol granulometry)	WMO: C-M-U
τ_{AER} (Aerosol Opt. Thickness at 500 nm)	0.1, 0.4
H_{AER} (Aerosol height e-folding)	2 km
n_{H2O} (relative air-water refractive index)	1.334
$\rho_w[\lambda]$ (Marine reflectance)	Model: Babin + Nechad
w (Wind speed)	5 m/s
n_{max} (Maximum order of scattering)	20
I_{pd} (Polarization flag)	1 (consider polarization)

III. METHODS

A. Simulations

The algorithm was tested on a simulated dataset, generated using the SOS v5.0 (Successive Orders of Scattering) radiative transfer code [12]. SOS is designed to solve the RT equation in plane-parallel environments on terrestrial or marine surfaces. In our simulations, the marine reflectance is composed of: i) a bidirectional component that simulates water-air surface, and ii) a lambertian component that accounts for radiation that interacts with the in-water constituents (also called *above-water reflectance*). To obtain the RC reflectances of the set, the code was run twice: 1) using the input values specified by Tab. I, and 2) assuming a black marine environment, and without aerosol content. The second set was subtracted to the first to compute the RC signal: $\rho_{RC}^{SOS} = \rho_{TOA}^{SOS}$[Air + Interface + Aerosols + Water reflectance] $- \rho_{TOA}^{SOS}$[Air + Interface].

This generated a total of 30750 RC reflectance spectra (Tab. I): 5 solar zenith angles, 5 viewing zenith angles, 5 azimuth angles, 3 aerosol granulometries and refractive indices (from the WMO models Continental, Maritime, Urban [24]), 2 aerosol optical depths at 500 nm and 41 water reflectances computed using Eqs. (7) and (8), with S varying logarithmically in the range $[0 - 1000]$ and fixing $X = 1$. Rayleigh scattering from air molecules is set according to Bodhaine *et al.* (1999) [3].

B. OLCI Imagery

OLCI L1B imagery were downloaded from Copernicus Online Data Access system on February 2017 [4]. Due to the fact that L2 products have not been released yet to the general public, RC reflectances from OLCI bands were processed manually with a homemade processor, following the next simple steps:

1) The L1B tof-of-atmosphere radiances (L_{TOA}) were converted to TOA reflectances (ρ_{TOA}):

$$\rho_{TOA} = \frac{\pi L_{TOA}}{E_S cos(\theta_S)} \qquad (10)$$

where E_S is the extra-atmospheric solar irradiance [18] and integrated using OLCI's SRFs.

2) A look-up-table of Rayleigh reflectances, ρ_R, is produced using the SOS RT code (which does not account for absorbing gases) for a nominal wind speed of $w = 5m/s$ for different sun-viewing geometries $(\theta_s, \theta_v, \Delta\phi)$ and subtracted to the TOA signal, generating the RC reflectances, ρ_{RC}:

$$\rho_{RC}[\lambda] = \rho_{TOA}[\lambda] - \rho_R(\theta_s, \theta_v, \phi, w = 5m/s)[\lambda] \quad (11)$$

3) A simple correction for O_3 and NO_2 absorption is done by applying a global transmittance factor $T^{O_3, NO_2}(\mu)[\lambda]$ to the RC reflectance, that depends on wavelength and the airmass coefficient, $\mu = \frac{1}{cos(\theta_s)} + \frac{1}{cos(\theta_v)}$:

$$\rho_{RC, gas-corr}[\lambda] = \frac{\rho_{RC}[\lambda]}{T^{O_3, NO_2}(\mu)[\lambda]} \quad (12)$$

where $T^{O_3, NO_2}(\mu)[\lambda] = e^{-k_{O_3}[\lambda][O_3]} e^{-k_{NO_2}[\lambda][NO_2]}$. Here, nominal concentrations were used: $[O_3] = 300DU$ and $[NO_2] = 1.1 \times 10^{16} part/cm^2$. The specific absorption properties were taken from the extinction factors $k_{O_3}[\lambda]$ and $k_{NO_2}[\lambda]$ tabulated at NASA-OBPG webpage [18].

C. In situ radiometric measurements

A total of 73 ASD-radiometric measurements were collected from several field campaigns done in Río de la Plata (Argentina/Uruguay) and were converted to water reflectance spectra to comparebetween the $BLR(\rho_w)$ computed from in-situ measurements and the $BLR(\rho_{RC})$ yielded by the reflectance model of Eqs. (7) and (8). The ASD-Spectroradiometer works in the spectral range of 350:1:2500 nm and was used to measure upwelling and downwelling radiances at reciprocal zenithal angles of $\theta = \pm 40$ and downwelling irradiance inferred from measuring nadir radiance at a quasi-lambertian plaque. [11].

IV. RESULTS

A. Evidence from OLCI L1B imagery

Fig. 1 shows an OLCI scene of the Belgian Coast from August 13th, 2016, together with $BLR(\rho_{RC})[620, 709, 779]$. This magnitude exhibits a near zero value in clear waters (far from the influence of the Scheldt Estuary, seen as darker in the RGB composite) and non-zero values in regions of turbid waters. It is noted that the sign of a $BLR(\rho_{RC})$ in a particular pixel has to do with the convexity of the RC reflectance triplet: negative (positive) BLRs mean positive (negative) convexities, i.e. negative as well as positive values are expected. This image is affected by a hazy atmosphere, appreciated as a grayish foreground on the RGB composite and also from the RC reflectances (see Fig. 2); but the $BLR(\rho_{RC})[620, 709, 779]$ values remain unaffected by this feature.

Fig. 2 illustrates: i) how the three $BLR(\rho_w)$ vary according to water reflectance at $1016nm$. (upper insets, in-situ modelled and simulated data), compared to ii) how $BLR(\rho_{RC})$ vary according to RC reflectance at 1016 nm (lower insets, OLCI scenes). For $BLR(\rho_w)$ values, in situ ASD data were plotted
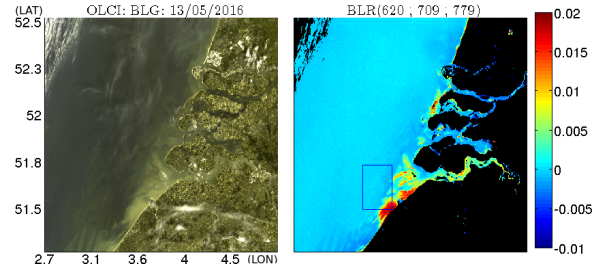

Fig. 1. Left: OLCI scene from the Belgian Coast on Aug 13th, 2016 (RC RGB Composite). Right: $BLR(\rho_{RC})[620, 709, 779]$, showing near-zero values for clear waters. Land and cloud masks are shown in black. Subset marked with blue rectangle is plotted in Fig. 2.
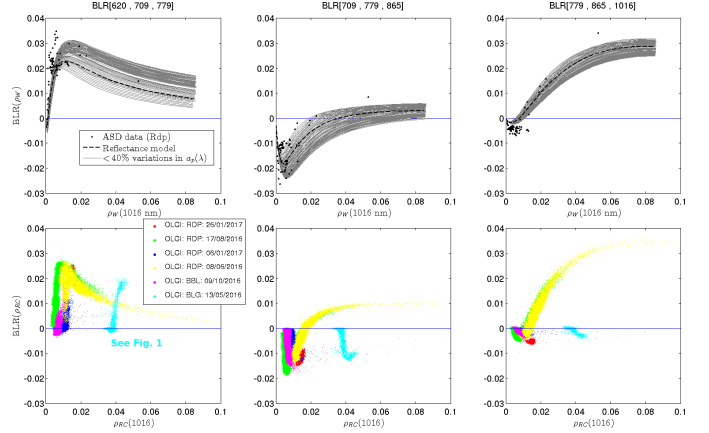

Fig. 2. Comparing $BLRs$ from different sources. Upper insets: $BLR(\rho_w)$ from in-situ ASD spectra (black dots) and modelled reflectances vs. $\rho_w(1016)$ (dashed line: Babin sIOPS, grey lines: X variations considered, see Eq. 8). Lower insets: $BLR(\rho_{RC})$ from OLCI scenes vs. $\rho_{RC}(1016)$.

(black dots), as well as the modelled curves (where S varied logarithmically in [0 - 1000] mg/L and X varies in the range [0.6−1.4]). In the three cases, $BLR(\rho_w)$ behave similarly with increasing reflectance. They all start from 0 towards negative values until they all reach a minimum negative value at a certain water reflectance. In these regimes, b_{bp} is still small, thus, neglecting the second order effect of a_p and the spectral dependence of b_{bp}, Eq. 1 is essentially in the case where $\rho_w[\lambda] \propto \frac{1}{a_w[\lambda]}$, giving negative convexities.

In the lower insets, this behavior is reproduced in a very similar fashion, but now for $BLR(\rho_{RC})$ derived from particular turbid sub-scenes from OLCI imagery of Río de la Plata (RDP), Bahía Blanca (BBL, Argentina) and Belgian Coast (BLG). As $\rho_{RC}[1016]$ are used as x-values, the different horizontal shifts from zero are attributed to different aerosol contents/sunglint present in the imagery. A subset of $BLR(\rho_{RC})$ from the very hazy image of Belgian waters showed in Fig. 1 is plotted in cyan. Observe how the haziness in the image has a great impact in the RC reflectances (x shift), while $BLR(\rho_{RC})$ remains quite unaffected by this condition.

B. Simulations

In Fig. 3, simulated $BLR(\rho_{RC})$ are plotted against modelled $BLR(\rho_w)$ (see §III-A). It is important to notice that,
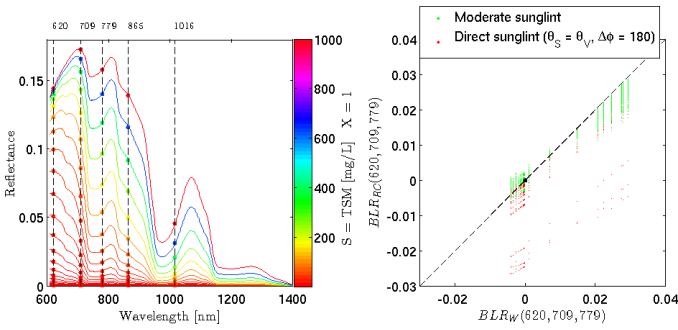
Fig. 3. Left: Modelled water reflectances (input to SOS). Right: Computed $BLR(\rho_{RC})$ vs. modelled $BLR(\rho_w)$.
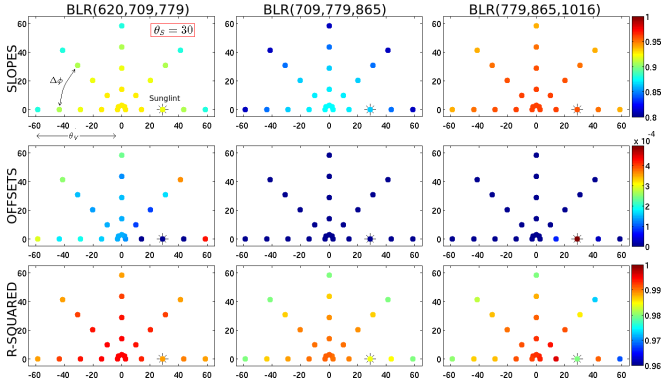

Fig. 4. Slopes (diffuse transmittances, $t[\lambda_M]$, Eq. 6), offsets, and R^2 retrieved by linear fit of simulated $BLR(\rho_{RC})$ vs. modelled $BLR(\rho_w)$ for all viewing geometries considered. Only scenarios with $\theta_s = 30$ are plotted.

in the cases where direct sunglint occurred (when $\theta_S = \theta_V$ and $\Delta\phi = 180$) simulated RC reflectances presented negative unexpected values, and also highly aerosol-dependent spectral behavior, meaning uncorrelated BLRs. This is associated to a significant increase in multiple scattering effects in the atmosphere which may maximize errors in the RT computations and also in the basic assumptions on aerosol properties when working with WMO models.

In general, $BLR(\rho_{RC})$ are slightly diminished in absolute value with respect to $BLR(\rho_w)$ as the signal propagates through the atmosphere, meaning a spectral smoothing of the radiance coming from inside the water body. This is in agreement with how we expect the atmosphere to interact with the signal coming from the water inside each BLR-triplet: as a near-white term that diminishes the signal in roughly the same amount for all bands, conveying the corresponding $BLR(\rho_{RC})$ to be reduced proportionally (Eq. 6). This equivalent transmittance factor (or gain factor) was calculated using a linear regression scheme for every subset of simulations corresponding to each sun-viewing geometry (where N = 246 for each of these subsets). Fig. 4 shows the results of this regression for all the viewing geometries, with solar zenith angle fixed at $\theta_s = 30$. Three quantities are plotted for each BLR and viewing angles: gains, offsets and R^2 of fit.

Notice that, in all cases, gains/transmittances are less than
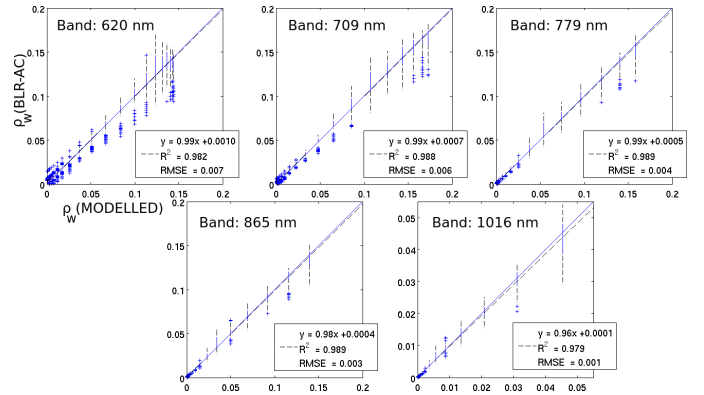

Fig. 5. Water reflectances retrieved by the atmospheric correction algorithm (BLR-AC) applied to simulated RC reflectances vs. input water reflectances from model (§II-A). Direct sunglint cases excluded.

1 but above 0.8. Lowest values are achieved in high viewing zenithal angles (outer dots), where the atmospheric path is maximized. Furthermore, offset values are generally less than 0.0001 and less than 0.0005 in all cases, i.e., small with respect to the typical BLR values exhibited in Fig. 2. The greatest offsets (lowest gains) are computed for BLR(620, 709, 779).

Fig. 5 shows the performance of the atmospheric correction scheme applied to the simulated dataset (direct sunglint cases excluded). For each modelled water reflectance inside each subplot, a boxplot was performed, where the interquartile zone is represented as a vertical blue line, the minimum/maximum range (excluding outliers) is plotted using a dashed black vertical line, and outliers are represented as blue "+" signs. Generally, performances are good, as represented with near-zero offsets (≤ 0.0010), near-unity slopes (≥ 0.96), high R^2 coefficients (≥ 0.97) and RMSE values less than 0.007.

C. Applying the algorithm to preliminary OLCI L1B imagery

Fig. 6 shows a preliminary result of the atmospheric correction scheme applied over the OLCI image of Río de la Plata on Jan 6th, 2017. Inset b) shows water reflectance at $1016nm$ retrieved by applying the BLR scheme. The values retrieved (in the range $[0 - 0.1]$) are consistent with the ones usually observed in Río de la Plata [11]. The turbidity front usually found in the oceanic-fresh water boarder is seen in front of the Buenos Aires Province (Argentina) as the most reflective feature of the scene (between Pins 3 and 4). All pins show realistic water and residual retrievals, including Pin 1 at the coast, which is located at Fishermen's Pier of Palermo (Buenos Aires), commonly used as validation site.

V. CONCLUSIONS

An atmospheric correction scheme was proposed for OLCI imagery over very turbid waters to retrieve water reflectances at bands centered at 620, 709, 779, 865 and 1016 nm. The scheme is based on: i) Computing for each pixel three "baseline residual" (BLR) quantities (Eq. 1) from the Rayleigh-corrected (RC) reflectances at the five aforementioned bands.
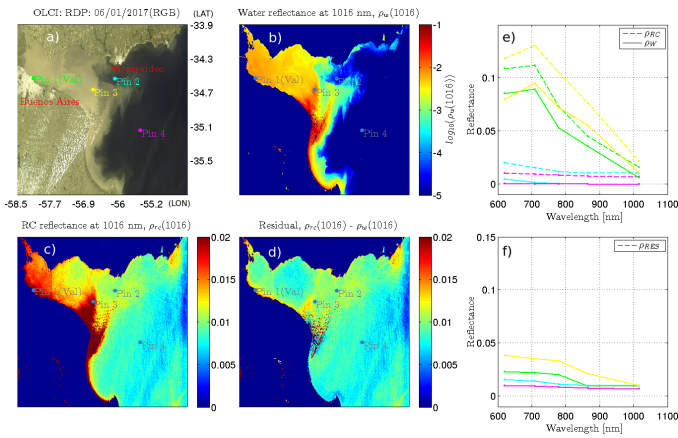
Fig. 6. Results of applying the atmospheric correction to the image of Río de la Plata on Jan 6th, 2017. a) RC RGB composite. b) Retrieved water reflectance at $1016nm$. c) RC reflectance at $1016nm$. d) Residual reflectance at $1016nm$ ($\rho_{RC}[1016nm] - \rho_w[1016nm]$). e) RC and water reflectances for selected pins. f) Same for residual reflectances.

These quantities are essentially independent on the atmospheric conditions. ii) Correcting the $BLR(\rho_{RC})$ values with a pre-computed diffuse transmittance factor $t(\lambda_M)$ at each pixel to obtain $BLR(\rho_w)$ and iii) associating $BLR(\rho_w)$ to a particular previously-modelled water reflectance spectrum in the RED/NIR/SWIR. To obtain these modelled spectra, particulate IOPs were varied proportionally to suspended matter concentration, and an extra parameter was considered to account for particulate absorption variability [20]. The main hypotheses of the algorithm were addressed in many ways: First, showing how these $BLR(\rho_{RC})$ behave inside a particular image. Second, comparing $BLR(\rho_{RC})$ from OLCI scenes to $BLR(\rho_w)$ from modelled and in-situ measured water reflectances. Third, evaluating the algorithm performance with a simulated RC dataset. BLRs from all sources considered behave in a similar way and are observed to be essentially conserved after the water leaving radiance interacts with the atmosphere. An effective transmittance factor was computed for the simulated dataset for each sun-viewing geometry. The performance of the algorithm was tested on the simulated dataset, yielding almost 1:1 regressions between RC and water reflectances for all five bands considered, with R^2 values above 97%. It was also tested on OLCI L1B imagery from Río de la Plata, yielding realistic spectra for water reflectances and uncorrelated residual and water signals, even without vicarious calibration of the sensor.

REFERENCES

[1] Babin, M., Morel, A., Fournier-Sicre, V., Fell, F., Stramski, D. (2003). Light scattering properties of marine particles in coastal and open ocean waters as related to the particle mass concentration. *Limnology and Oceanography*, 48, 843859.

[2] Babin, M., Stramski, D., Ferrari, G. M., Claustre, H., Bricaud, A., Obolensky, G., et al. (2003). Variations in the light absorption coefficients of phytoplankton, nonalgal particles and dissolved organic matter in coastal waters around Europe. *Journal of Geoph. Res.*, 108(C7), 3211.

[3] Bodhaine, B. A.,Wood, N. B., Dutton, E. G., Slusser, J. R. (1999) On Rayleigh Optical Depth Calculations. *Journal of Atmospheric and Oceanic Technology*, vol. 16.

[4] Copernicus Online Data Access, EUMETSAT: *www.coda.eumetsat.int*

[5] Dogliotti, A.I., Ruddick, K., Nechad, B., and Lasta, C. (2011). Improving Water Reflectance Retrieval from MODIS Imagery in the Highly Turbid Waters of La Plata River. Proceedings of VI International Conference: Current problems in optics of natural waters (ONW 2011). Publishing House Nauka of RAS, 2011. p. 152. Russia. 6-10 September.

[6] Dogliotti, A.I., K.G. Ruddick, B. Nechad, D. Doxaran, E. Knaeps (2015) A single algorithm to retrieve turbidity from remotely-sensed data in all coastal and estuarine waters, *R. Sens. of Environment*, Vol. 156, 157-168

[7] Dogliotti, A.I., K. Ruddick, R. Guerrero, Seasonal and inter-annual turbidity variability in the Ro de la Plata from 15 years of MODIS: El Nio dilution effect, Estuarine, Coastal and Shelf Science, Volume 182, 2016, Pages 27-39, ISSN 0272-7714

[8] ESA Sentinel 3 Online, website: *http://www.sentinel.esa.int*

[9] Gordon, H. R., Wang, M. (1994), Retrieval of Water-Leaving Radiance and Aerosol Optical Thickness over the Oceans with SeaWiFS: A Preliminary Algorithm., *Applied Optics*, 33, 443-452.

[10] Hu, C. (2007) A novel ocean color index to detect floating algae in the global oceans. *Remote Sensing of Environment*, 113 21182129.

[11] Knaeps, E and Dogliotti, A.I, Raymaekers, D, Ruddick, K and Sterckx, S (2012) In situ evidence of non-zero reflectance in the OLCI 1020 nm band for a turbid estuary. *Remote Sensing of Environment*, 10.1016

[12] Lenoble, J., M. Herman, J.L. Deuz, B. Lafrance, R. Santer, D. Tanr (2007). A Successive Order of Scattering Code for Solving the Vector Equation of Transfer in the Earth's Atmosphere with Aerosols. *Journal of Quantitative Spectroscopy & Radiative Transfer* 107 479-507.

[13] Letelier, R. M., Abott, M. R. (1996). An analysis of chlorophyll fluorescence algorithms for the Moderate Resolution Imaging Spectrometer (MODIS). *Remote Sensing of Environment*, 58, 215 - 223.

[14] Loisel, H., Morel, A. (2001). Non-isotropy of the upward radiance field in typical coastal (Case 2) waters. *International Journal of Remote Sensing*, 22(2 & 3), 275295.

[15] Mobley, C. D. (1994). Light and water: radiative transfer in natural waters. *London: Academic Press*.

[16] Moreira, D., C. G. Simionato, F. Gohin, F. Cayocca, M. L. Clara Tejedor, Suspended matter mean distribution and seasonal cycle in the Ro de La Plata estuary and the adjacent shelf from ocean color satellite (MODIS) and observations, *Continental Shelf Research*, Volume 68, 2013, Pages 51-66, ISSN 0278-4343.

[17] Morel, A., Gentili, B. (1996). Diffuse reflectance of oceanic waters. III. Implication of bidirectionality for the remote-sensing problem. *Applied Optics*, 35(24), 48504862.

[18] NASA Goddard Space Flight Center, Ocean Biology Processing Group, website: https://oceancolor.gsfc.nasa.gov/

[19] Nechad, B., K.G. Ruddick, Y. Park, Calibration and validation of a generic multisensor algorithm for mapping of total suspended matter in turbid waters, Remote Sensing of Environment 114 (2010) 854866

[20] Pinet, S., Martinez, J.M., Ouillon, S., Lartiges, B., Espinoza Villar, R. (2017). Variability of apparent and inherent optical properties of sediment-laden waters in large river basins lessons from in situ measurements and bio-optical modeling. *Opt. Express* 25, A283-A310.

[21] Ruddick, K.G., Vanhellemont, Q. (2015) Use of the new OLCI and SLSTR bands for atmospheric correction over turbid coastal and inland waters. Submitted for the proceedings of the Sentinel-3 for Science Workshop held in Venice-Lido, Italy, 2-5 June 2015, ESA Special Publication SP-734.

[22] Stumpf, R. P., R. A. Arnone, J. R. W. Gould, P. M. Martinolich, and V. Ransibrahmanakul (2003), A Partially Coupled Ocean-Atmosphere Model for Retrieval of Water-Leaving Radiance from SeaWiFS in Coastal Waters. *NASA Tech. Memo. 206892*.

[23] Wang, M., Shi, W., (2007). The NIR-SWIR Combined Atmospheric Correction Approach for MODIS Ocean Color Data Processing. *Opt. Express* 15, 15722-15733.

[24] World Climate Research Programme (1986) A Preliminary Cloudless Standard Atmosphere for Radiation Computation, WCP 112, WMO/TD Report No 24, Geneva, Switzerland , March 1986